NUMERICAL SIMULATIONS OF THE AEROELASTIC BEHAVIOR OF LARGE HORIZONTAL–AXIS WIND TURBINES: THE DRIVETRAIN CASE

Cristian Gebhardt[a,b,c]**, Badrinath Veluri**[b]**, Sergio Preidikman**[a,c]**, Henrik Jensen**[b] **and Julio Massa**[a]

[a]*Structures Department, Córdoba National University, 1611 Vélez Sarsfield Av, 5000 Córdoba, Argentina,*
cgebhardt@efn.uncor.edu, http://www.efn.uncor.edu

[b] *Mechanical Engineering Department, Aarhus University, 4 Dalgas Avenue, 8000 Aarhus, Denmark,*
vb@agse.dk, http://www.iha.dk

[c] *CONICET, Rivadavia Av. 1917, CP C1033AAJ Buenos Aires, Argentina, http://www.conicet.gov.ar*

Abstract. In this work an aeroelastic model that describes the interaction between aerodynamics and drivetrain dynamics of a large horizontal–axis wind turbine is presented. Traditional designs for wind turbines are based on the output of specific aeroelastic simulation codes. The output of these codes gives the loads acting on the wind turbine components caused by external forces such as the wind, the electricity grid and (for offshore applications) sea waves. Since the focus in the traditional codes lies mainly on the rotor loads and the dynamic behavior of the overall wind turbine, the model of the drive train in the wind turbine is reduced to only a few degrees of freedom. This means that, for the design of the drive train, the simulated load time series need to be further processed to applied loads on the individual components, such as gears and bearings. Furthermore, the limitation of the model implies that vibrations of these internal drive train components are not taken into account and, as a consequence, dynamic loads on these components cannot be simulated. In this effort an aerodynamical model based on the non–linear and unsteady vortex–lattice method is used to compute the aerodynamic loads and their evolution in the space and the time domains, considering multiple aerodynamic interactions among blades, wakes, hub, nacelle, support tower, ground and land–surface boundary layer. All these in combination affect substantially the total efficiency of the turbine. In addition, a flexible multibody model for the drivetrain is developed as a way to include directly the high speed shaft's (which connects the gear box and generator) flexibility. For the inter–model combination, a strong interaction scheme based on the fourth order Hamming predictor–corrector method is used. The models and the interaction scheme are implemented in a computational tool; using this tool, the behavior of the turbine in the starting initial regime is investigated considering different laws of brake releasing. The capability to simulate these phenomena is a novel aspect in the present effort.

1. INTRODUCTION

Due to increasing environmental concern, and approaching limits to fossil fuel consumption, alternative and clean sources of energy have regained interest. Among the several energy sources being explored, wind energy −a form of solar energy− shows much promise in selected areas of North Europe and South America where the average wind speeds are high.

Utilization of the energy in the winds requires the development of devices which convert that energy into more useful forms. Wind turbines are used to generate electricity from the kinetic energy of the wind. In order to capture this energy and convert it to electrical energy, one needs to have a device capable of "touching" the wind. This device, or turbine, is usually composed of three major parts: the 'rotor blades', the drivetrain and the generator. The blades are the part of the turbine that touches the wind and rotates about an axis.

Energy extraction from the wind is typically accomplished by first mechanically converting the velocity of the wind into a rotational motion of the wind turbine by means of the rotor blades, and then converting the rotational energy of the rotor blades into electrical energy using a generator. The amount of available energy which the wind transfers to the rotor depends on the mass density of the air, the sweep area of the rotor blades, and the wind speed, and total amount of energy extracted from the airstream by the wind turbine strongly depends on its aerodynamic efficiency (Gebhardt et al., 2010).

The overall aim of this work is to develop a fundamental understanding of the nonlinear and unsteady interaction between aerodynamics and drivetrain dynamics of a large horizontal− axis wind turbine (LHAWT). To render this understanding, a comprehensive computational tool is been developed, and the understanding gained through this study will is been used for predicting the responses of LHAWTs (Gebhardt et al., 2009). The computational tool consists of the following three principal elements: *i*) an aerodynamical model, *ii*) a drive-train dynamical model, and *iii*) a scheme for inter−model combination to numerically solve all of the governing equations, interactively in the time domain (Preidikman, 1998; Preidikman et al., 2010).

The aerodynamical model is based on the non−linear and unsteady vortex−lattice method (NLUVLM), (Konstandinopoulos et al., 1981; Katz and Plotkin, 2001) this is a well−known technique in subsonic aerodynamics. The used version of NLUVLM was expanded to take in account the wake−tower interaction and the land−surface boundary layer. The drivetrain dyna- mical model is very simple, nevertheless the flexibility of the high speed shaft (HSS) which connects the gear box and generator is considered. For the inter−model combination, a strong interaction scheme based on a modified version of the fourth order Hamming predictor− corrector method is used (Carnahan et al., 1969; Preidikman, 1998).

Since, the aim is to study general unsteady behavior and also explore nonlinear phenomena, the simulations are carried out in the time−domain. It is expected these numerical tool will provide the accuracy needed during the design, development, testing, and deployment of LHAWT.

2. THE AERODYNAMICAL MODEL

2.1. The mathematical problem

Consider a 3D incompressible flow of an inviscid fluid generated due to the unsteady motion of the rotor blades. The absolute velocity of a fluid particle which occupies the position $\mathbf{R}$ at instant t is denoted by $\mathbf{V}(\mathbf{R};t)$. Since the flow is irrotational outside the boundary layers and

the wakes, the velocity field can be expressed as the gradient of a total velocity potential $\Phi(\mathbf{R};t)$ as:

$$\mathbf{V}(\mathbf{R};t) = \nabla\Phi(\mathbf{R};t) \tag{1}$$

The spatial/temporal evolution of the total velocity potential is governed by the continuity equation for incompressible flows.

$$\nabla^2\Phi(\mathbf{R};t) = 0 \tag{2}$$

A set of boundary conditions (BCs) must be added (Preidikman, 1998; Gebhardt et al., 2009). The location of the body's surface is known, possibly as a function of time, and the normal component of the fluid velocity is prescribed on this boundary. The first BC requires the normal component of the velocity of the fluid relative to the body to be zero at the boundaries of the body. This BC, commonly called the "no−penetration or impermeability" BC (on the surface of the solid surface), becomes:

$$(\mathbf{V} - \mathbf{V}_S)\cdot\hat{\mathbf{n}} = (\nabla\Phi - \mathbf{V}_S)\cdot\hat{\mathbf{n}} = 0 \tag{3}$$

where $\mathbf{V}_S$, is the velocity of the boundary surface S, and $\hat{\mathbf{n}}$ is the unit normal vector.

In general, $\mathbf{V}_S$ and $\hat{\mathbf{n}}$ vary in space and time. A regularity condition at infinity must also be imposed. This second BC requires that the flow disturbance, due to the motion of the body (or bodies) through the fluid, should diminish far from the body. This is usually called the regularity condition at infinity and is given by

$$\lim_{\|\mathbf{R}\|_2\to\infty}\left\|\mathbf{V}(\mathbf{R};t)\right\|_2 = \lim_{\|\mathbf{R}\|_2\to\infty}\left\|\nabla\Phi(\mathbf{R};t)\right\|_2 = \left\|\mathbf{V}_\infty\right\|_2 \tag{4}$$

where $\mathbf{V}_\infty$, is the non−perturbed free stream velocity and $\|\ \|_2$ denotes the vector 2−norm.

Since the disturbated velocity field is computed according to the Biot−Savart law, the regularity condition at infinity is satisfied identically. For incompressible potential flows, the velocity field is determined from the continuity equation, and hence, it may be established independently of the pressure.

Once the velocity field is known, the pressure is calculated from the unsteady Bernoulli equation. Moreover, since the speed of sound is assumed to be infinite, the influence of the BCs is immediately radiated across the whole fluid region; therefore, the instantaneous velocity field is obtained from the instantaneous BCs. In addition to the BCs, the Kelvin−Helmholtz theorems (Lugt, 1983) and the unsteady Kutta condition are used to determine the strength and position of the wakes.

The integral representation of the velocity field $\mathbf{V}(\mathbf{R};t)$ in terms of the vortex field $\mathbf{\Omega}(\mathbf{R};t)=\nabla\times\mathbf{V}(\mathbf{R};t)$, is an extension of the well−known Biot−Savart law. For 3D flows, it takes the following form:

$$\mathbf{V}(\mathbf{R};t) = \frac{1}{4\pi}\iint_{S(\mathbf{R}_0;t)}\frac{\mathbf{\Omega}(\mathbf{R}_0;t)\times(\mathbf{R}-\mathbf{R}_0)}{\|\mathbf{R}-\mathbf{R}_0\|_2^2}\,dS(\mathbf{R}_0;t) \tag{5}$$

where $\mathbf{R}_0$, is a position vector on the compact region $S(\mathbf{R}_0;t)$ of the fluid domain. The integrand in the surface integral (5) is zero wherever $\mathbf{\Omega}(\mathbf{R};t)$ vanishes. Thus, the region where the flow

is irrotational does not contribute to **V** anywhere. **V** can be evaluated explicitly at each point, i.e., independently of the evaluation of **V** at neighboring points. As a consequence of this feature, which is absent in finite difference methods, the evaluation of **V** can be confined to the viscous region; the vorticity distribution in the viscous region determines the flow field in both, the viscous and inviscid regions.

In order to formulate the no−penetration BC given by Equation (3) it is convenient to divide the total velocity potential $\Phi(\mathbf{R};t)$ into three parts, the first one due to the bound− vortex sheet Φ_B, the second due to the free−vortex sheet Φ_W and the last due to the free stream Φ_∞. Hence, Equation (3) can be rewritten as:

$$\left(\nabla\Phi_B + \nabla\Phi_W + \nabla\Phi_\infty - \mathbf{V}_S\right)\cdot\hat{\mathbf{n}} = 0 \tag{6}$$

2.2. The non−linear and unsteady vortex−lattice method

In the NLUVLM, the continuous bound−vortex sheets are discretized into a lattice of short, straight vortex segments of constant circulation $\Gamma_j(t)$. These segments divide the surface of the body into a number of area elements. The model is completed by joining free vortex lines, representing the continuous free−vortex sheets, to the bound−vortex lattice along the edges of separation; such as the trailing edges and tips of the rotor blades.

Experience with the vortex−lattice method suggests that the geometric shape of the elements in the lattice affects the accuracy and the rate of convergence. It was found that rectangular elements work better than other shapes (Preidikman, 1998). Consequently, as much as possible we use rectangular, or nearly rectangular, elements everywhere except in those places where we are forced to use triangular elements: for example, at the hub of the windmill.

Each element of area in the lattice is enclosed by a loop of vortex segments. To reduce the size of the problem, we can consider each element to be enclosed by a closed loop of vortex segments having the same circulation. Then the requirement of spatial conservation of circulation is automatically satisfied. These loop circulations are denoted by $G_j(t)$.

Because the vortex sheets are approximated by a lattice, the no−penetration condition given by Equations (3) or (6) can be satisfied at only a finite number of points, the so−called control points. The control points are the centroids of the corner points (aerodynamic nodes).

The problem consists of finding the circulations $G_j(t)$ around the discrete vortices on the bound−lattice such that the velocity field **V** satisfies conditions (3) or (6) at the control points. In order to find these circulations, we construct a matrix of aerodynamic influence coefficients A_{ij} for $i,j = 1,2,\ldots,NP$ where NP is the number of elements (closed loops of constant vorticity) in the bound lattice. The coefficient A_{ij} represents the normal component of the velocity at the control point of the i−th element associated with a unit circulation around the vortex of element j−th, and is in general a function of time. In terms of the coefficients A_{ij} (Konstandinopoulos et al., 1981; Katz and Plotkin, 2001), the no−penetration condition given by Equation (6) can be written as follows:

$$\sum_{j=1}^{NP} A_{ij} G_j(t) = -\left[\nabla\Phi_W + \nabla\Phi_\infty - \mathbf{V}_B\right]_i \cdot \hat{\mathbf{n}}_i \qquad i = 1,2,\ldots,NP \tag{7}$$

The algebraic linear system of equations given by Equation (7) is used to compute the unknown circulations $G_j(t)$. At the end of each time step, to satisfy the Kutta condition, vorticity is shed into the flowfield and become part of the grids that approximate the free

vortex sheets of the wake. Because the vorticity in the wake at a given time was generated on, and shed from, the body at an earlier time, the flowfield is history–dependent and so the current distribution of vorticity on the surface of the body depends to some extent on the previous distributions of vorticity.

The vorticity distribution and the shape of the wake are determined as part of the solution so the history of the motion is stored in the wake. We say that the wake is the 'historian' of the flow. As time passes the vorticity in the wake convects far downstream so its associated velocity field has negigible influence on the flow around the body; thus, the historian has a fading memory. In the numerical method, this means that only the wake near to the body is important; the rest can be safely neglected.

The method developed in this effort treats the position of, and the distribution of vorticity in, the wakes as unknown and they are determined as part of the solution. The present method employs an explicit routine for generating the unsteady wake, instead of the iterative scheme that was used previously by some investigators (Kandil et al., 1976), providing efficiency without a loss of accuracy and even providing solution for some cases where the iterative methods did not converge.

To generate the wakes, the discrete vortex segments at the trailing edge and the tip of each rotor blade are convected at the local particle velocity, $\mathbf{V}[\mathbf{R}(t)]$, calculated from the Biot–Savart law. The updated positions, $\mathbf{R}(t+\Delta t)$ of the vortex points are computed according to:

$$\mathbf{R}(t+\Delta t) = \mathbf{R}(t)+\Delta \mathbf{R}(t) \approx \mathbf{R}(t)+\mathbf{V}\big[\mathbf{R}(t)\big]\Delta t \qquad (8)$$

This approximation for the value of $\Delta \mathbf{R}(t)$ does not need iterations and is stable (Kandil et al., 1976).

In a previous work, Gebhardt et al. (2009; 2010) expanded the NLUVLM, including two new capabilities in the current model, by developing and implementation of a wake rupture procedure and a land-surface boundary layer model. The first one allows taking into account, with a satisfactory agreement, the effects produced due to the interactions between the wakes and the tower, and the second one allows accounting the losing efficiency due to a realistic wind profile. A visualization of a functioning LHAWT, and the time evolution of its wakes, is presented in Figure 1.

2.3. Loads computation

The aerodynamics loads acting on the lifting surfaces (rotor blades) are computed as follows: *i*) the pressure jump at the control point of each element is computed from the unsteady version of Bernoulli Equation (9); *ii*) the force at each area element is computed as the product among the pressure jump times the area of the element times the unit normal vector; *iii*) the resultant force and moment are computed as the vector addition of the forces and moments produced by each element.

$$\frac{\partial \Phi}{\partial t}+\frac{1}{2}\mathbf{V}\cdot\mathbf{V}+\frac{p}{\rho} = \frac{1}{2}\mathbf{V}_\infty\cdot\mathbf{V}_\infty+\frac{p_\infty}{\rho_\infty} \qquad (9)$$

The details of each term of Equation (9) are shown in references Konstandinopoulos et al. (1981), Preidikman (1998) and Preidikman and Mook (2005).
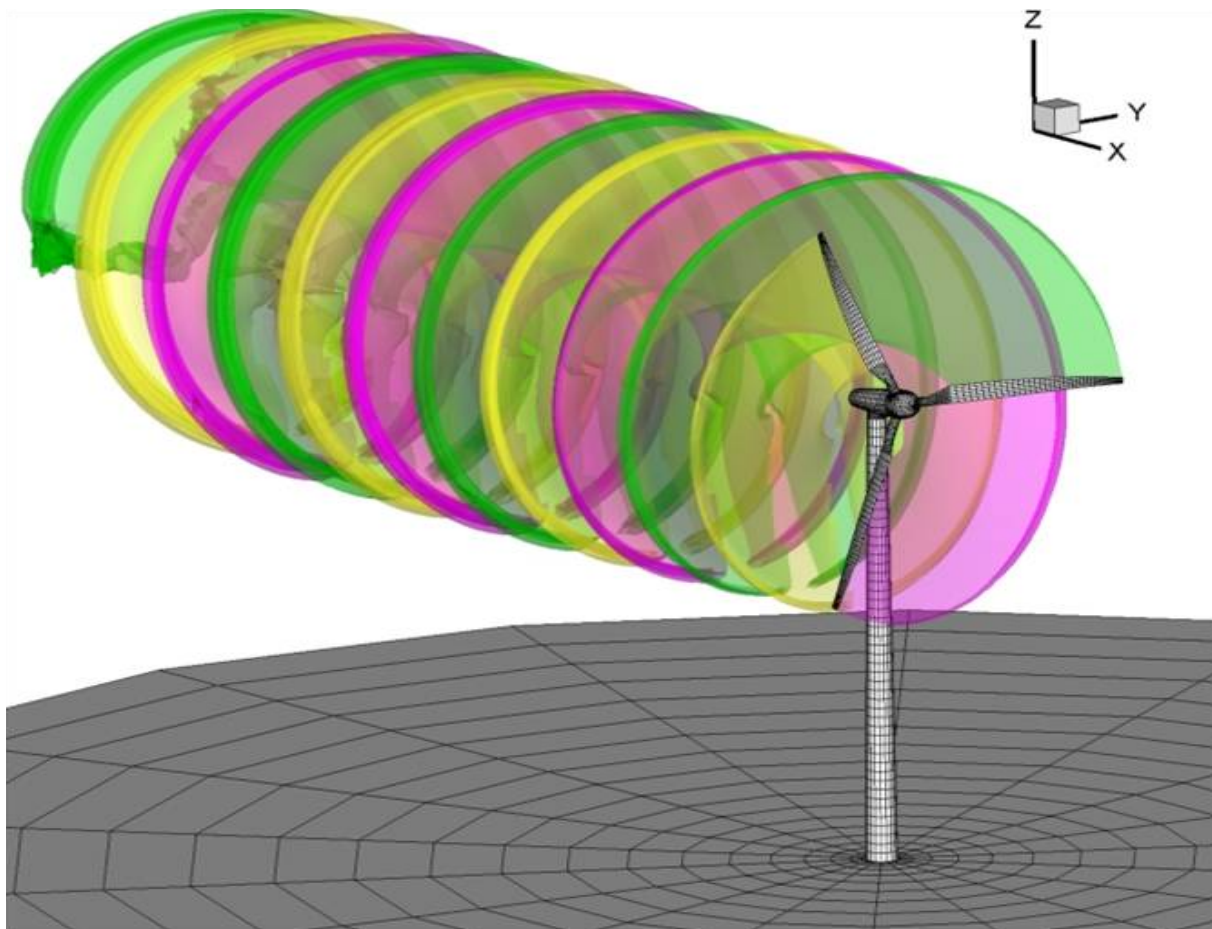
Figure 1: Evolution of the wakes emanating from a LHAWT.

3. THE DRIVETRAIN MODEL

The aerodynamic torque on the drivetrain of a LHAWT varies continuously over the time due to the unsteady and non-linear characteristics of the complex aerodynamics. The variations are directly transferred to the dynamic mechanical transmission system. The electrical generator runs at a relatively high speed compared to the aerodynamic rotor. In the drivetrain a low speed shaft (LSS) in the rotor side is connected to a HSS in the electrical generator side by using a gearbox.

Real installations are continua with infinite degrees of freedom, but a detailed investigation with a reduced number of DOF is, as a rule, entirely sufficient for analyzing their dynamic behavior. Consequently, it is desirable to develop a mathematical model that reflects the relevant features of the real technical system as accurately as possible. Any restrictions on movement (linkages) between the bodies are realized with joints with specific properties. Such mechanical systems are described mathematically by coupled ordinary differential and algebraic equations. In general a simulation model must first of all satisfy the following requirements:

1. The model must represent the conditions of the real system as accurately as possible.

2. The connection between the real system and the reduction in the model should be noticeable at each point.

3. It should be possible to calculate the system parameters on which the model is based from the technical documents or from the real system itself with sufficient accuracy.

3.1. Mathematical modelling of the drivetrain system

A reduced 2-DOF model with simple inertia representation of the drivetrain containing the gear box is shown in Figure 2. In this model the rotor, gears and LSS are treated as rigid bodies while the HSS is considered as a flexible body.
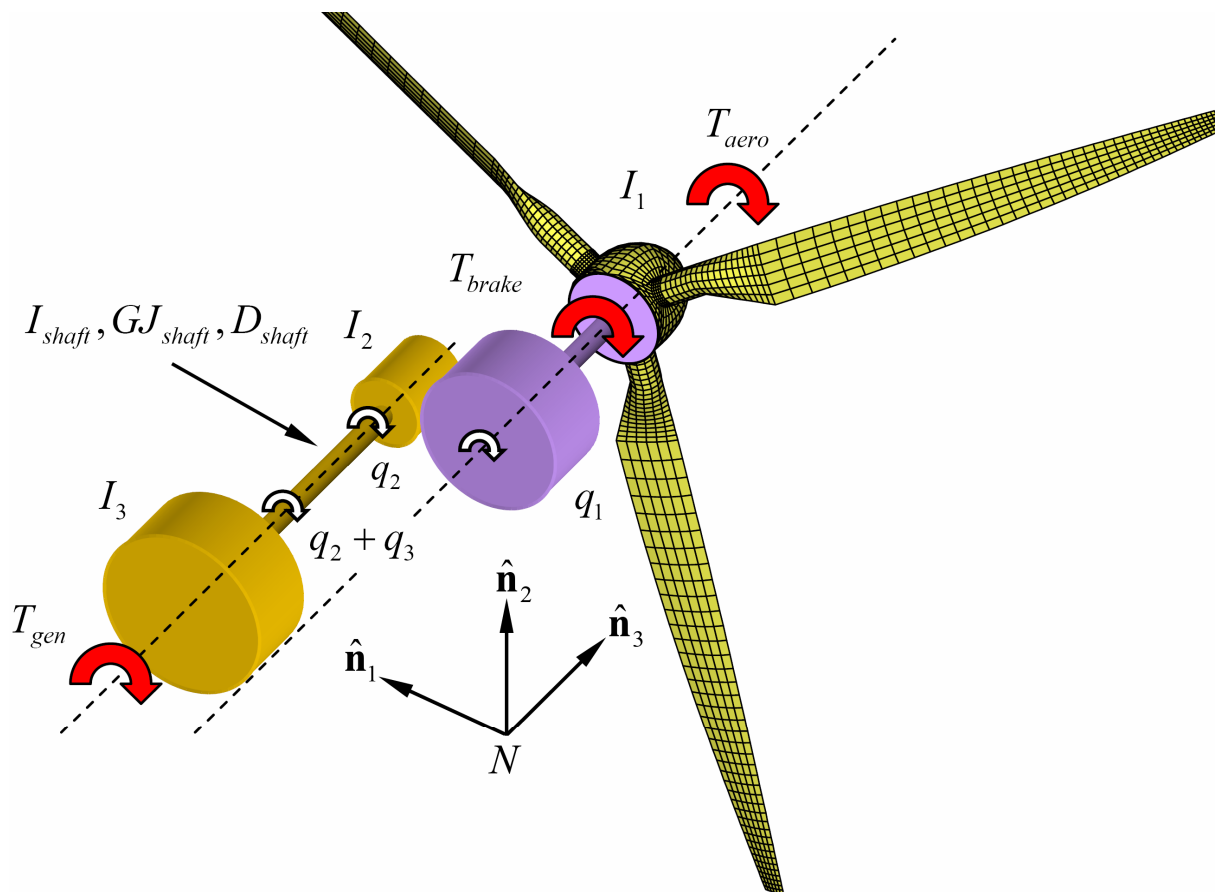
Figure 2: A reduced dynamic representation of LHAWT drivetrain.

The tangential velocity vector at the contact point for the first gear expressed in the fixed reference frame N is given by:

$$\mathbf{v}_1^T = \boldsymbol{\omega}_1 \times \mathbf{r}_1 = \left\{ \dot{q}_1(t)\,\hat{\mathbf{n}}_3 \right\} \times \left\{ r_1\,\hat{\mathbf{n}}_1 \right\} = \dot{q}_1(t)\,r_1\,\hat{\mathbf{n}}_2 \tag{10}$$

where $\dot{q}_1$ and r_1 are the angular velocity and the radius of the first gear, respectively.

The tangential velocity at the contact point for the second gear is expressed in N as:

$$\mathbf{v}_2^T = \boldsymbol{\omega}_2 \times \mathbf{r}_2 = \left\{ \dot{q}_2(t)\,\hat{\mathbf{n}}_3 \right\} \times \left\{ -r_2\,\hat{\mathbf{n}}_1 \right\} = -\dot{q}_2(t)\,r_2\,\hat{\mathbf{n}}_2 \tag{11}$$

where $\dot{q}_2$ and r_2 are the angular velocity and the radius of the second gear, respectively.

At the contact point the tangential velocity must to be equal for both gears ($\mathbf{v}_1^T = \mathbf{v}_2^T$), and the constraint relation becomes:

$$\dot{q}_1(t)\,r_1 + \dot{q}_2(t)\,r_2 = 0 \quad \Rightarrow \quad \dot{q}_2(t) = -n_g\,\dot{q}_1(t) \tag{12}$$

where $n_g = r_1/r_2$ is the gear ratio.

The kinetic energy, T, of the system can be expressed as:

$$T = \frac{1}{2}I_1\left[\dot{q}_1(t)\right]^2 + \frac{1}{2}I_2\left[\dot{q}_2(t)\right]^2$$
$$+ \frac{1}{2}I_3\left[\dot{q}_2(t) + \psi(L)\dot{q}_3(t)\right]^2 + \frac{1}{2}\int_0^L I_{shaft}(\eta)\left[\dot{q}_2(t) + \psi(\eta)\dot{q}_3(t)\right]^2 d\eta \tag{13}$$

where $\dot{q}_3$ is the torsional deformation velocity spanned by the shape function ψ over all the shaft length I_1, I_2 and I_3 are the rotational inertias for the rotor and first gear, second gear, and the generator, respectively. And I_{shaft} is the shaft's rotational inertia distribution per unit length.

The system's potencial energy can be expressed as:

$$U = \frac{1}{2}\int_0^L GJ_{shaft}(\eta)\left[\psi'(\eta)q_3(t)\right]^2 d\eta \tag{14}$$

where GJ_{shaft} is the shaft's torsional stiffness per unit length.

Using Lagrange's equations, virtual work principle for external and damping loads, the constraint relation, and assuming $\psi(\eta) = \eta/L$ compatible with the shaft's boundary conditions relative to the rigid body motion and assuming constant shaft's section and properties, the equations of motion for the system are (Baruh, 1999; Tenenbaum, 2004):

$$[\mathbf{M}]\{\ddot{\mathbf{q}}\} + \left[\dot{\mathbf{M}} + \mathbf{D}\right]\{\dot{\mathbf{q}}\} + [\mathbf{K}]\{\mathbf{q}\} = \{\mathbf{F}\} \tag{15}$$

where $\{\mathbf{q}\}$ is the configuration vector which contains the generalized coordinates, $[\mathbf{M}]$ is the mass matrix, $[\dot{\mathbf{M}}]$ is the first time derivative of the mass matrix, $[\mathbf{D}]$ is the damping matrix, $[\mathbf{K}]$ is the stiffness matrix, and $\{\mathbf{F}\}$ is the vector of generalized forces.

The intervening vectors and matrices in the equations of motion (15) are expressed as:

$$\{\mathbf{q}\} = \left\{ q_3 \quad q_3 \right\}^T \tag{16}$$

$$[\mathbf{M}] = \begin{bmatrix} I_1 + n_g^2\left(I_2 + I_3 + I_{shaft}L\right) & -n_g\left(I_3 + I_{shaft}L\right) \\ -n_g\left(I_3 + I_{shaft}L\right) & I_3 + I_{shaft}L \end{bmatrix} \tag{17}$$

$$\left[\dot{\mathbf{M}} + \mathbf{D}\right] = \begin{bmatrix} \dot{I}_1 & 0 \\ 0 & 0 \end{bmatrix} + \begin{bmatrix} 0 & 0 \\ 0 & D_{shaft} \end{bmatrix} = \begin{bmatrix} \dot{I}_1 & 0 \\ 0 & D_{shaft} \end{bmatrix} \tag{18}$$

$$[\mathbf{K}] = \begin{bmatrix} 0 & 0 \\ 0 & \dfrac{GJ_{shaft}}{L} \end{bmatrix} \tag{19}$$

$$\{\mathbf{F}\} = \left\{ \begin{matrix} T_{aero} - n_g T_{gen} + T_{brake} \\ T_{gen} \end{matrix} \right\} \tag{20}$$

where D_{shaft} is the HSS damping, T_{aero}, T_{gen} and T_{brake} are aerodynamical, generator and braking torques, respectively. And $\dot{I}_1$ is the first time derivative of I_1 which varies as the pitching angle of the blades changes.

Consider a controlled torque brake which releases the LSS proportionally with the aerody-namical torque increment by a time dependant factor β, it means that the torque due to the brake can be written as:

$$T_{brake} = -\beta\, T_{aero} \tag{21}$$

Therefore, the first component of the vector $\mathbf{F}$ can be expressed as:

$$\{\mathbf{F}\}_1 = (1-\beta)T_{aero} - n_g\, T_{gen} = \gamma\, T_{aero} - n_g\, T_{gen} \tag{22}$$

In general $\gamma = 1 - \beta$ is the brake releasing function which depends on the time, and T_{gen} is related to the angular velocity of HSS.

4. COMBINING THE MODELS

In current investigations, the aerodynamics and dynamics are treated as the elements of a single dynamical system. All the governing equations are solved simultaneously and interac-tively in the time domain. The methodology is based on a fourth order predictor–corrector method developed by Hamming (Carnahan et al., 1969). In the late nineties this method was adapted and expanded to solve fluid–structure interaction problems (Preidikman, 1998).

However, this methodology presents an obstacle: to predict the dynamic effects on the drive-train system, the aerodynamic loads must be known. To overcome this obstacle, an iterative scheme is being developed to account for the interaction among aerodynamic loads, drivetrain dynamics and control systems. The interaction scheme proposed based on the above mentioned model to solve all the governing equations in the time domain is presented in Figure 3.
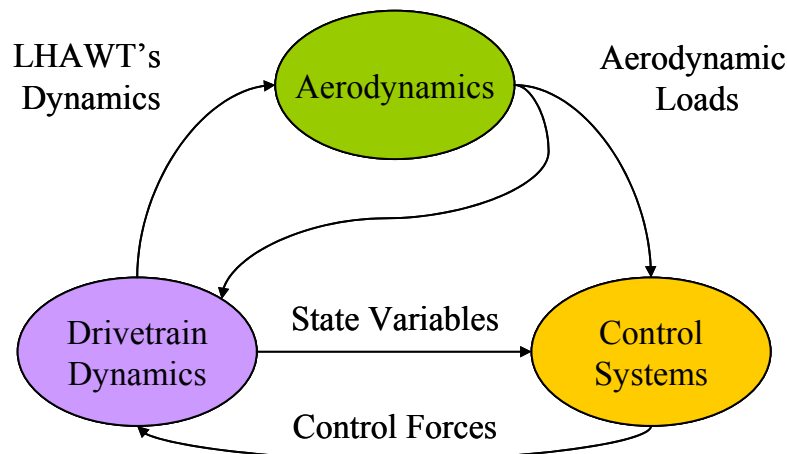
Figure 3: Combining the models.

4.1. The numerical–integration scheme

The differential equations of motion can be written as a first order differential equation system:

$$\dot{\mathbf{y}}(t) = \mathbf{F}[\mathbf{y}, \dot{\mathbf{y}}, t, \tau], \qquad 0 \le \tau \le t \tag{23}$$

where $\mathbf{y}(t) = \{\dot{\mathbf{q}}(t) \quad \mathbf{q}(t)\}^T$ is the estate vector and τ denotes history dependence.

Stages used by the integration algorithm:

Using a time step equal to Δt we solve numerically the system equations

$$\mathbf{y}^j \;=\; \mathbf{y}\left(t_j\right) \qquad \dot{\mathbf{y}}^j \;=\; \dot{\mathbf{y}}\left(t_j\right) \qquad \mathbf{F}^j \;=\; \mathbf{F}\left[\mathbf{y}\left(t_j\right), \dot{\mathbf{y}}\left(t_j\right), t_j, \tau_j\right] \tag{24}$$

were t_j is the time at j-th time step ($t_j = j\,\Delta t$).

1. At $t = 0$ the solution is obtained using initial conditions $\mathbf{y}^0$.

2. At $t = \Delta t$ the solution ${}^P\mathbf{y}^1$ is predicted using a first order algorithm, the explicit Euler method (Heath, 2002; Burden and Faires, 2005). By using the modified Euler method (Burden and Faires, 2005), the corrected solution ${}^1\mathbf{y}^1$ is obtained. This solution is iteratively corrected until it satisfies: $\left\| {}^{k+1}\mathbf{y}^1 - {}^k\mathbf{y}^1 \right\|_\infty < \varepsilon$, where k is the iterations number, ε is a tolerance and $\| \;\; \|_\infty$ denotes the vector infinity norm.

3. At $t = 2\Delta t$ the solution ${}^P\mathbf{y}^2$ is predicted using a second order algorithm, the two–steps Adams–Bashfort method (Burden and Faires, 2005). By using the two–steps Adams–Moulton method (Burden and Faires, 2005), the corrected solution ${}^1\mathbf{y}^2$ is obtained. This solution is iteratively corrected until it satisfies: $\left\| {}^{k+1}\mathbf{y}^2 - {}^k\mathbf{y}^2 \right\|_\infty < \varepsilon$.

4. At $t = 3\Delta t$ the solution ${}^P\mathbf{y}^3$ is predicted using a third order algorithm, the three–step Adams–Bashfort method (Burden and Faires, 2005). By using the three–steps Adams–Moulton method (Burden and Faires, 2005), the corrected solution ${}^1\mathbf{y}^3$ is obtained. This solution is corrected until it satisfies: $\left\| {}^{k+1}\mathbf{y}^3 - {}^k\mathbf{y}^3 \right\|_\infty < \varepsilon$. The local truncation error is computed as $\mathbf{e}^3 = {}^{k+1}\mathbf{y}^3 - {}^1\mathbf{y}^3$.

5. At $t = j\Delta t$, for $j \geq 4$ the solution ${}^P\mathbf{y}^j$ is predicted using a fourth order algorithm, the modified Hamming's method (Preidikman, 1998). The predicted solution is modified using the local truncation error computed in the previous time step. By using the modified Hamming's method the first corrected solution ${}^1\mathbf{y}^j$ is obtained. This solution is iteratively corrected until it satisfies $\left\| {}^{k+1}\mathbf{y}^j - {}^k\mathbf{y}^j \right\|_\infty < \varepsilon$ and the local truncation error $\mathbf{e}^j$ is computed. Finally the corrected solution is modified using $\mathbf{e}^j$. This solution is the final solution.

Iterations are necessary due to the strong fluid–structure interaction scheme. At each time step, the iterations are performed holding constant the positions and shapes of the wakes. The wakes are convected once the final solution reaches the convergence.

The integration's methodology presented in this study allows solving problems where acceleration terms are present on both sides of the governing equations, and the estimation of aerodynamic loads must be performed at integer multiples of the time steps. In the present problem solution, the aerodynamic loads computation represents the highest computing cost, and its estimation inside the time steps would be very expensive. This means that a Runge–Kutta method is not suitable for the present solution strategy.

5. RESULTS AND DISCUSSION

The present investigation was carried out for a standard 3 blades LHAWT with a rotor diameter of 78 m, tower height 80 m, and considering the following wind specifications: speed at 10 m of height 10 m/s (refrence for the land-surface boundary layer model); speed at the hub heigh 12,8 m/s, considering a flat terrain with very low building density as a rural zone. The accounted mesh specifications for the aerodynamical model are: the total number of elements 3952 which includes 456 for each blade, 864 for the hub, 496 for nacelle, 882 for the tower and 342 for the ground.

In the present effort, the case of study is focused on the impact of the non-linear and unsteady aerodynamic loads over the drivetrain at starting initial regime. In order to reach this target three diferent laws of brake releasing are proposed and investigated. The first one contains a step or Heaviside releasing law, the second one is a first order polynomial law with continuity C^0, and the last one is a third order polynomial law with continuity C^1. Where C^n denotes continuity of the function up to the n-th derivative. The three abovementioned laws of brake releasing are presented in Table 1 and plotted in Figure 4.

Table 1: Laws of brake releasing.

$\gamma(\tau)$	$\tau < 0$	$0 \leq \tau \leq 1$	$\tau > 1$
Heaviside	0	1	1
Poly 1	0	τ	1
Poly 3	0	$-2\tau^3 + 3\tau^2$	1

where $\tau = (t/t_{rel})$ and t_{rel} is the reference time at which the brake is completely released.
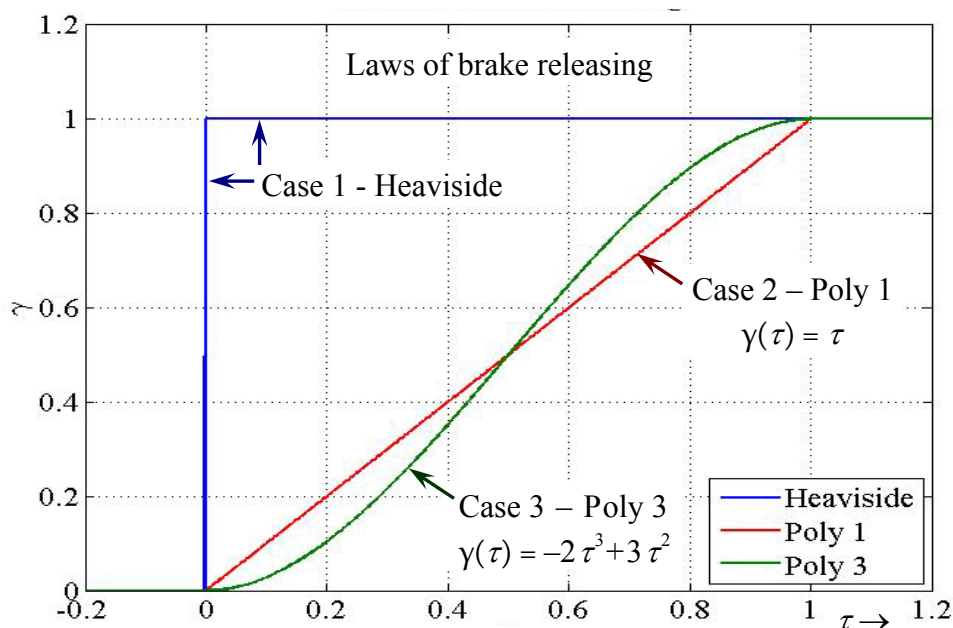
Figure 4: Three diferent laws of brake releasing used in the present study.

The results obtained with the computational tool for each one of the three braking law are discussed in following subsections. All the results are plotted as a function of the rotor azimuth angle in order to make a consistent comparison among the various studied cases.

5.1 Heaviside law of brake releasing

In Figures 5a, 5-b and 5-c, the results for the Heaviside law of brake releasing are presented.

In Figure5-a the angular velocity of the rotor $\dot{q}_1$ normalized with respect to the steady state angular velocity $\dot{q}_{1ss}$ and it is plotted as a function of the rotor azimuth angle q_1. The rotor angular speed increases gradually until it reaches the steady state (SS) angular velocity which was obtained numerically from the computational tool, this limit is due to the aerodynamical damping, and the 90 % of the SS angular velocity is reached after 20 revolutions.
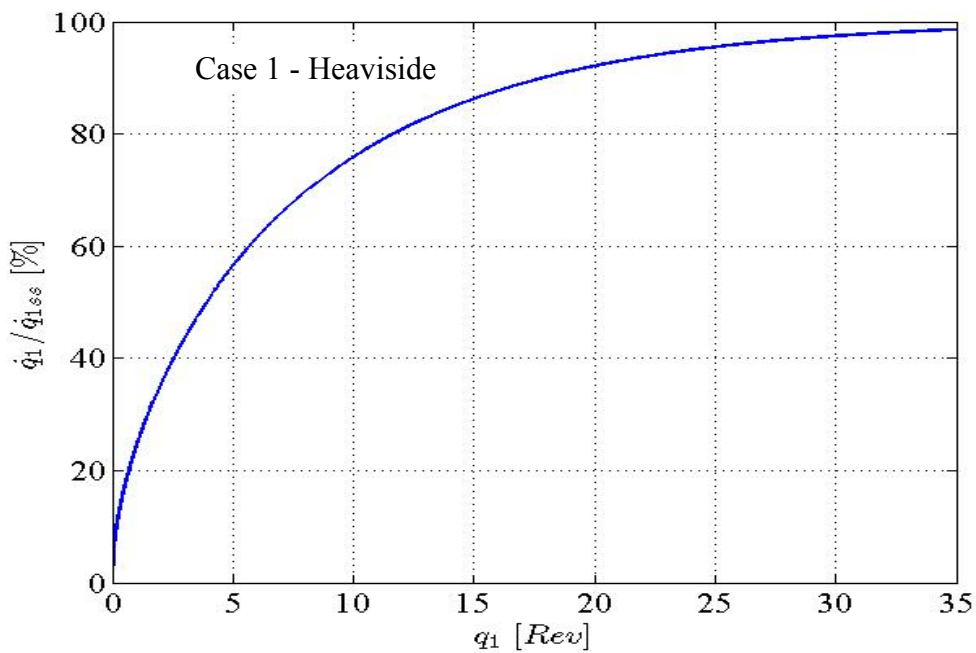
Figure 5-a: Normalized rotor angular velocity as for the Heaviside law of brake releasing.

In Figure 5-b the torsional angle of the HSS q_3 is plotted as a function of q_1. It is observed that the torsional angle increases drastically as an impact response due to the initial aerodynamical shock load, which is transmitted from the rotor because of the applied law of brake releasing. After a few rotor revolutions the decreasing trend is observed and finally it reaches the steady state value with the fluctuations coming from the elastic response of the HSS, and the unsteady effects due to support tower presence and land-surface boundary layer.
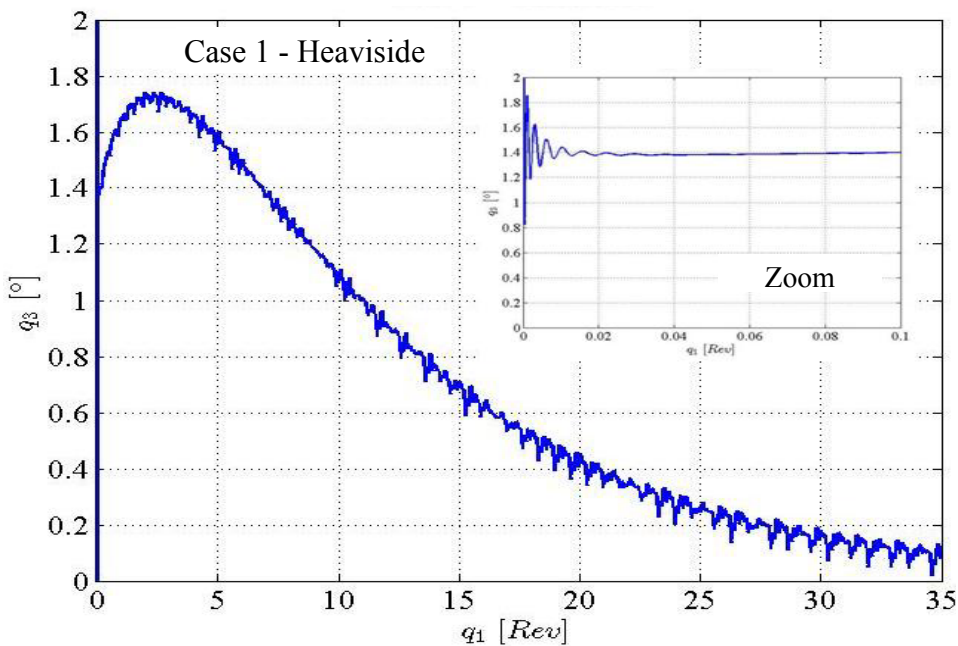
Figure 5-b: Torsional deformation angle of the HSS for the Heaviside law of brake releasing.

In Figure 5-c the torsional speed of the HSS $\dot{q}_3$ is plotted as a function of q_1. A shock response can be observed as an impact load on the HSS in the initial stage of releasing. Later

on, the fluctuations are consistent with the above mentioned. These fluctuations can have a considerable impact on fatigue life but it is not the subject of the present study. This phenomenon calls for further investigations.
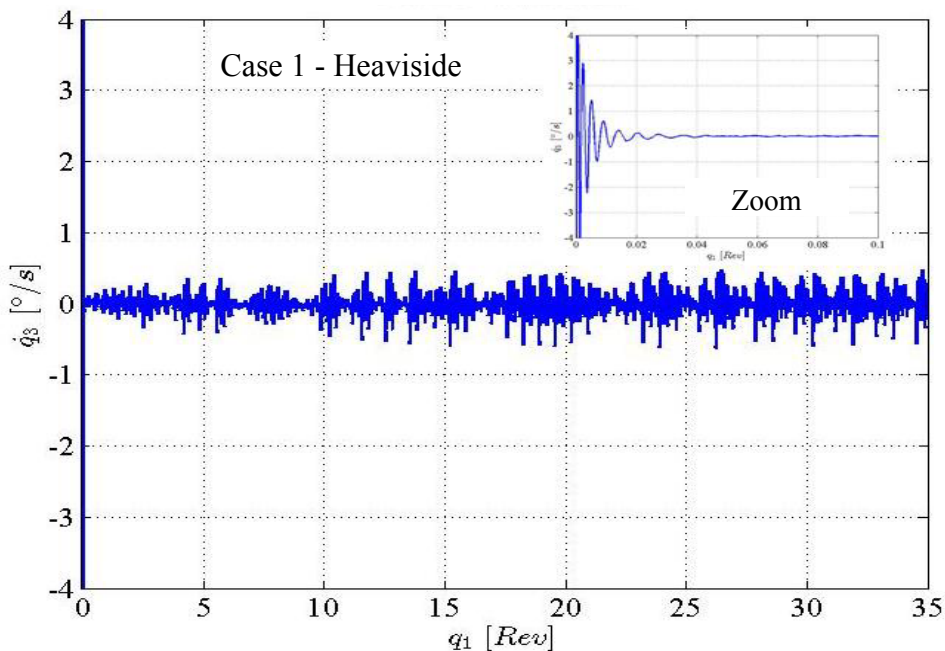
Figure 5-c: Torsional deformation speed of the HSS for the Heaviside law of brake releasing.

5.2. Poly 1 law of brake releasing

In Figures 6-a, b and c, the results for law Poly 1 of brake releasing are presented.

In Figure 6-a it can be observed that the rotor angular speed increases gradually until it reaches the SS angular velocity following the same trend as the previous case.
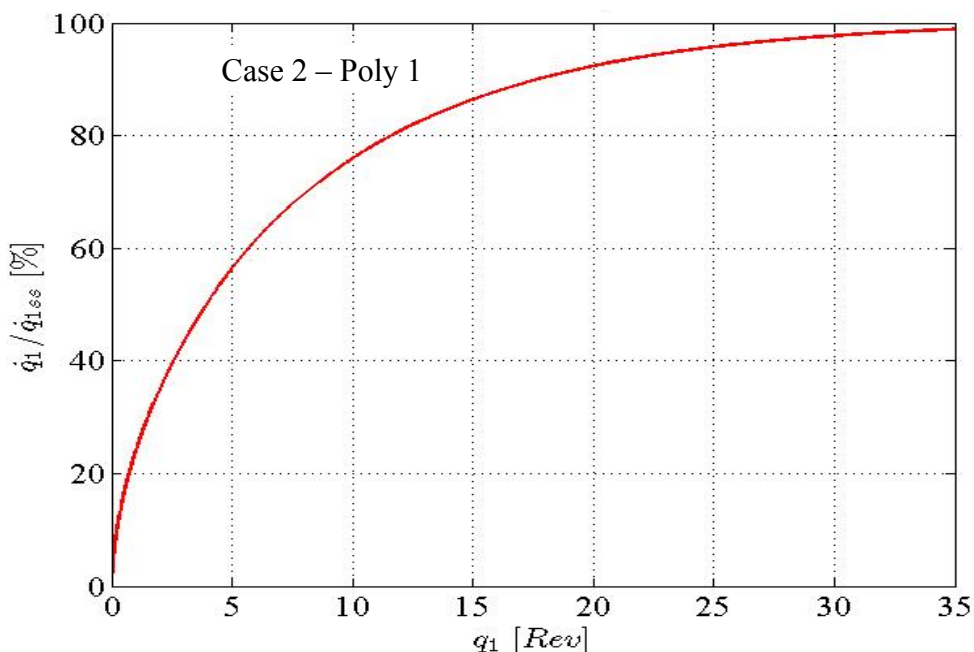
Figure 6-a: Normalized rotor angular velocity for the Poly 1 law of brake releasing.

Figure 6-b shows that q_3 has a no shock the impact response as observed in the Heaviside case at inicial stage wright after releasing, but after that it follows the same trend of the previous case.
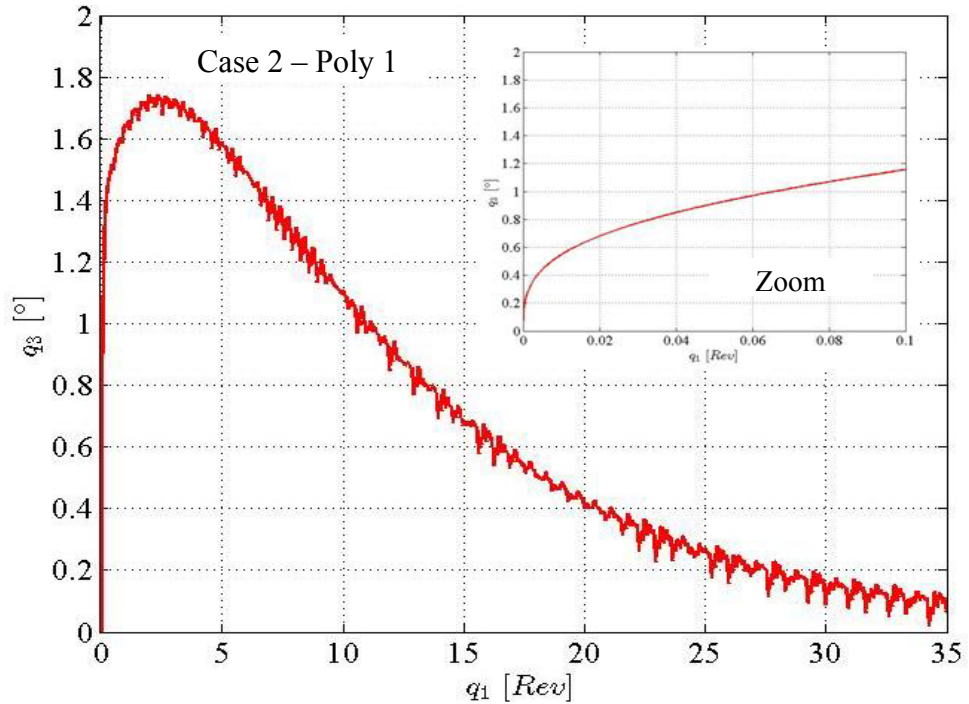
Figure 6-b: Torsional deformation angle of the HSS for the Poly 1 law of brake releasing.

In Figure 6-c, it can be observed that $\dot{q}_3$ presents consistent fluctuations with almost no shock response at the beginning of the initial stage.
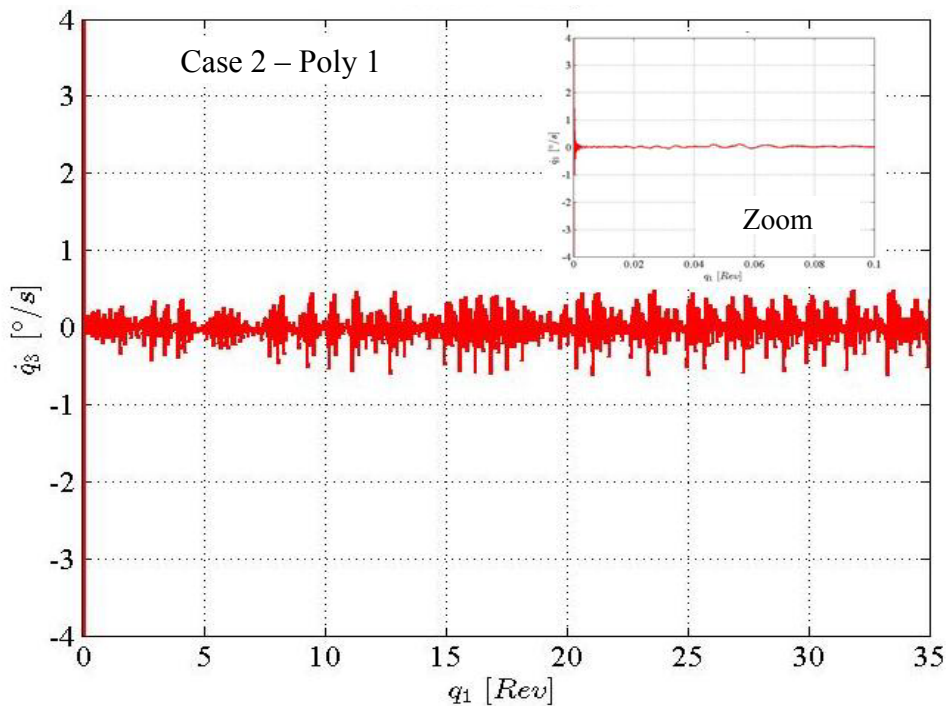
Figure 6-c: Torsional deformation speed of the HSS for law Poly 1 of brake releasing.

5.3. Poly 3 law of brake releasing

In Figure 7-a, b and c, the results of law Poly 3 for brake releasing are presented.

In Figure 7-a it can be observed that the rotor angular speed increases gradually until it reaches the angular velocity with the same trend of the previous cases.

In Figure 7-b, it can be confirmed that q_3 presents the same a trend similar to case Poly 1.
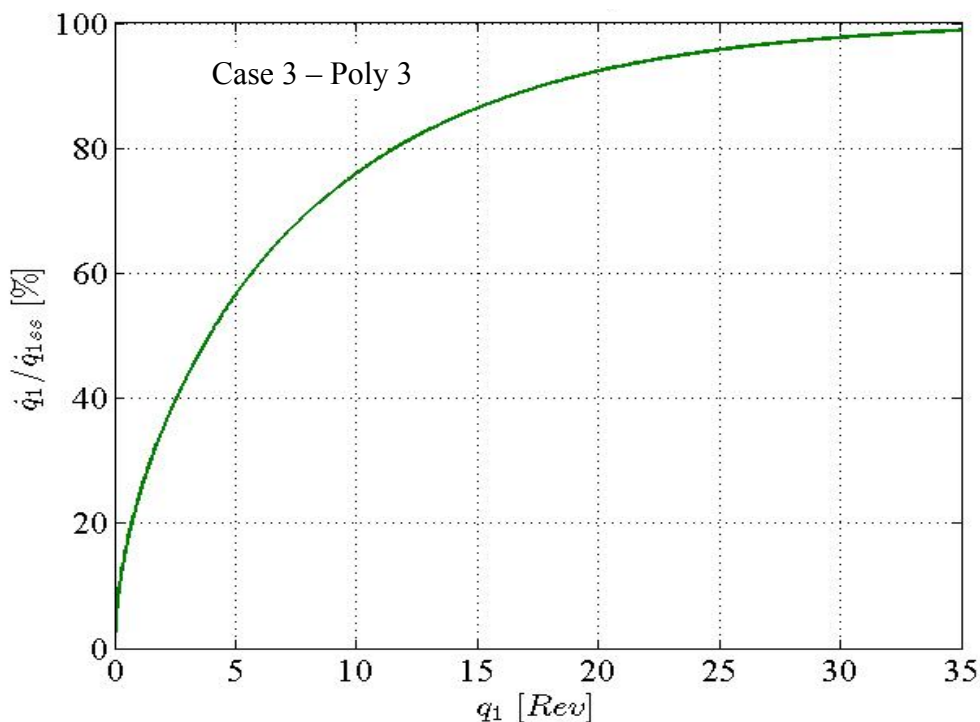
Figure 7-a: Normalize rotor angular velocity for the Poly 3 law of brake releasing.
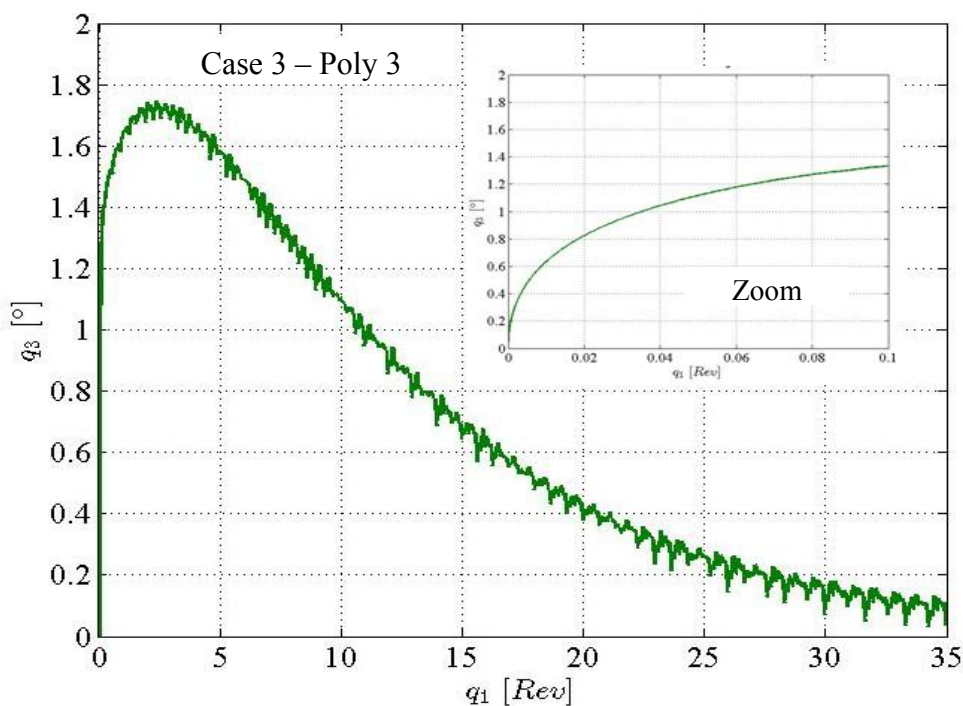
Figure 7-b: Torsional deformation angle of the HSS for the Poly 3 law of brake releasing.

In Figure 7-c, it can be confirmed that $\dot{q}_3$ presents consistent fluctuations, similar to case Poly 1.
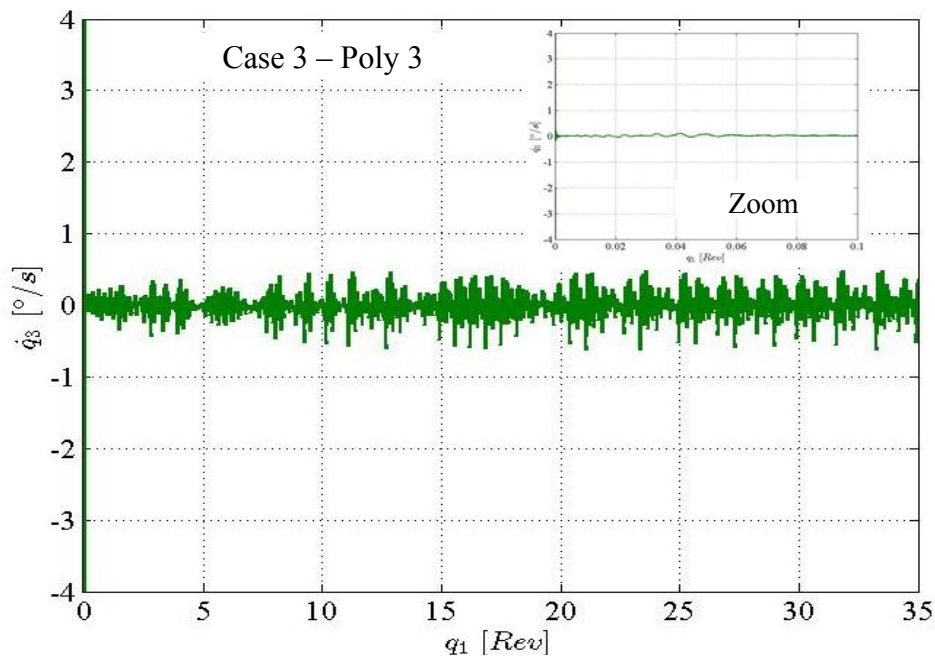
Figure 7-c: Torsional deformation speed of the HSS for the Poly 3 law of brake releasing.

5.4. Comparison for the three laws of brake releasing

A comparison study had been made among the three cases studied in the present investigation.

In Figure 8-a, the angular velocity $\dot{q}_1$ for all the three cases are plotted as a function of rotor azimuth angle q_1. It has been observed that the laws of brake releasing do not have a significant effect on the angular velocity of the rotor.
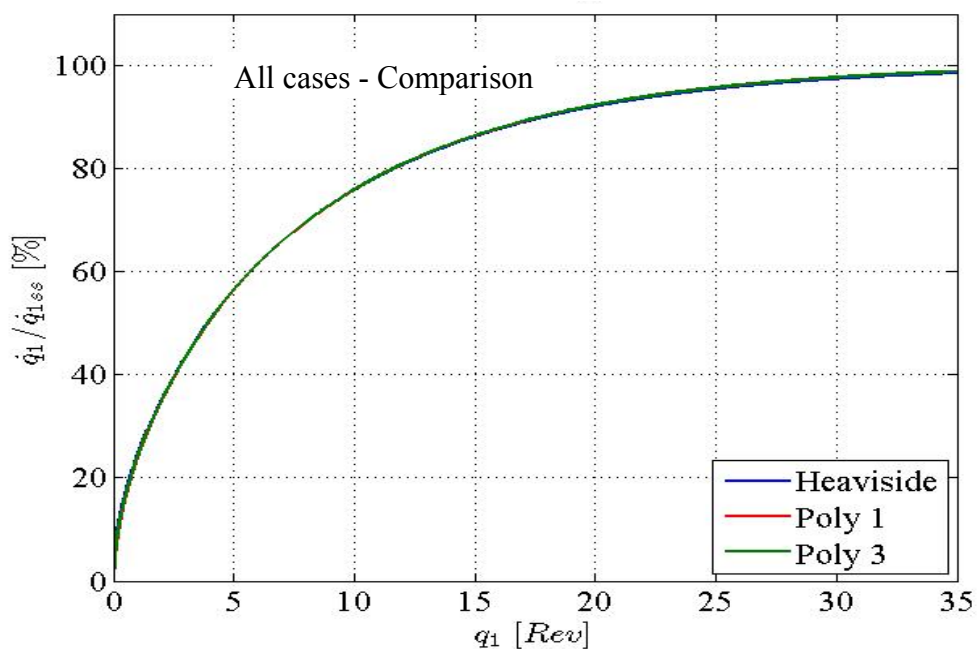
Figure 8-a: Normalized rotor angular velocity for the all cases.

In Figure 8-b and Figure 8-c the torsional angle of the HSS has a huge impact in the case of the Heaviside law of brake releasing. This study exposes the impact of shocks in the initial stage of the start regime has a considerable effect (due to the tipe of law of brake releasing). Figure 8-c is a zoom at initial time (less than one tenth of revolution) where it is shown that the responses of the system are quite diferent at the begining, but they rsapidly converges.
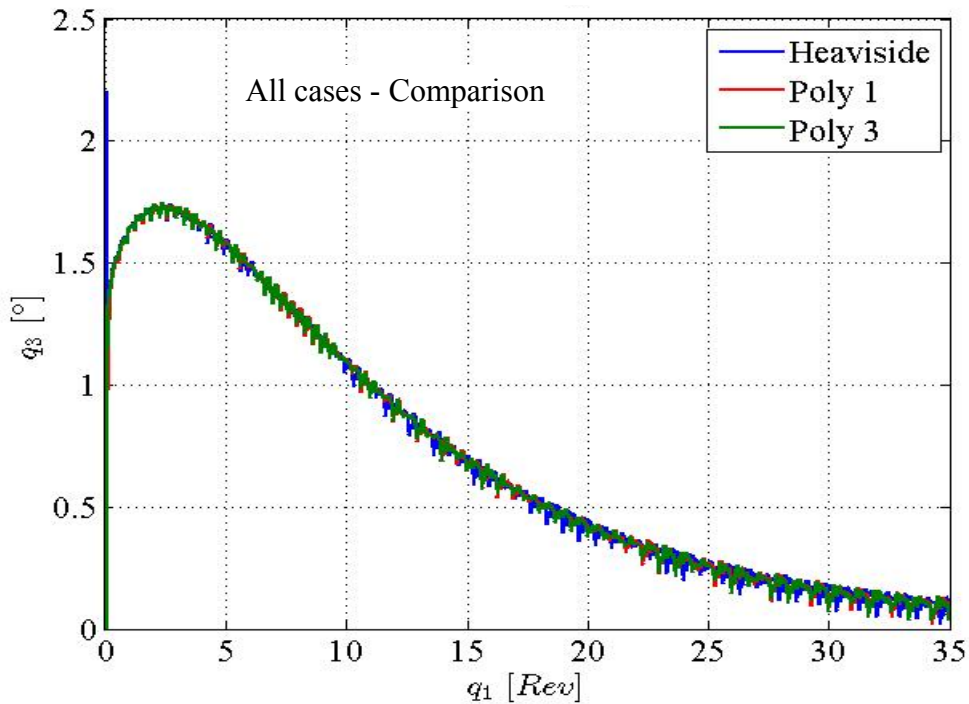
Figure 8-b: Torsional angle of the HSS for the all cases.
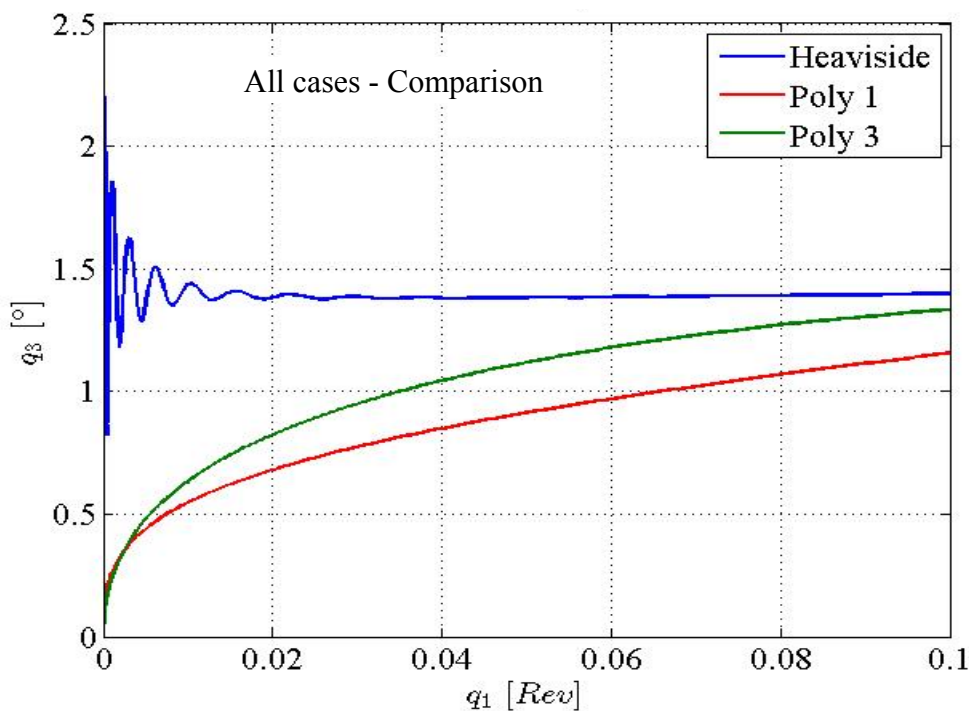
Figure 8-c: Torsional angle of the HSS for the all cases - zoom.

Figures 8-d and 8-e expose the impact of law of brake releasing on the HSS during the initial stages of the start regime which is in agreement with the previous statements of the present study. In Figure 8-e the Heaviside functions shows a huge fluctuating values of $\dot{q}_3$ and the in the other cases $\dot{q}_3$ shows a positive trend ($\dot{q}_3 > 0$) during the initial start transient. Later on, every case has a similar behavior.
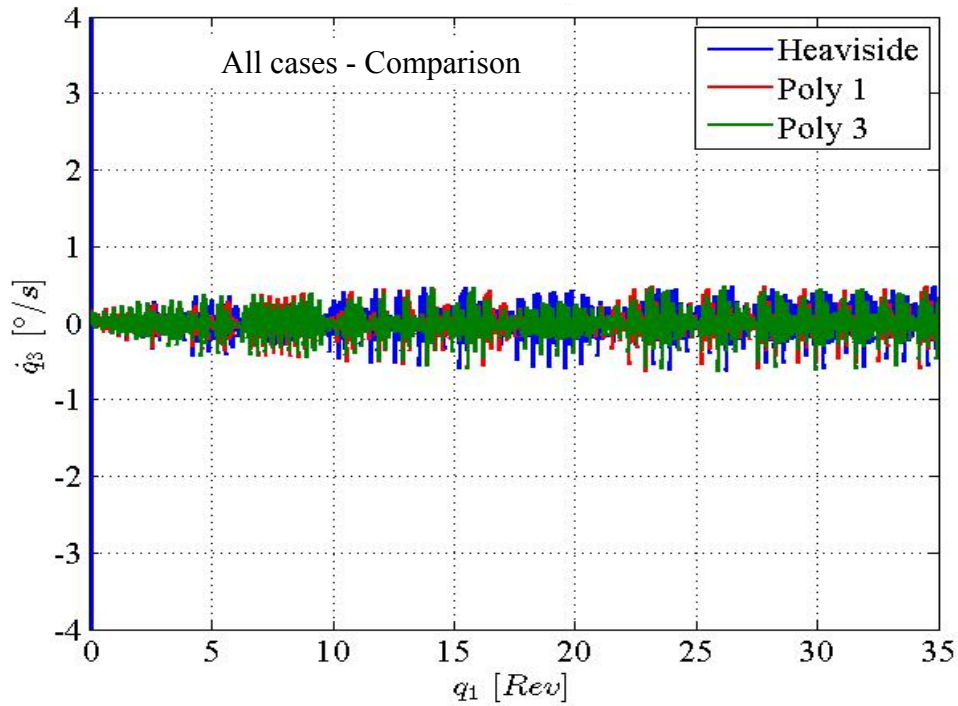
Figure 8-d: Torsional deformation speed of the HSS for the all cases.
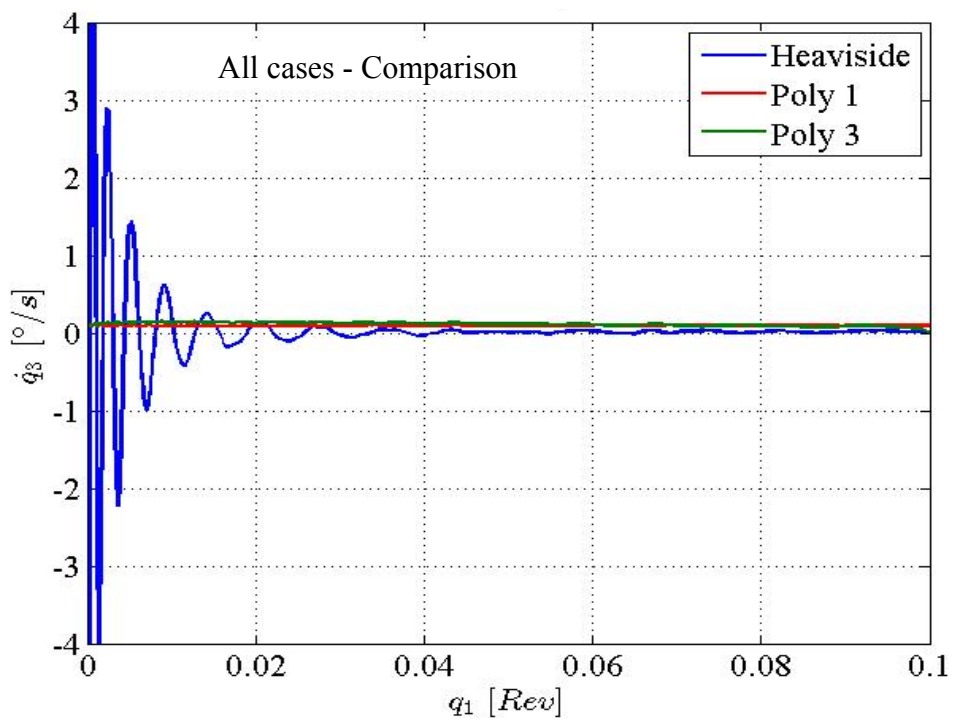
Figure 8-e: Torsional deformation speed of the HSS for the all cases.

6. CONCLUDING REMARKS

In this present work a novel methodology has been developed to study the dynamic effects of the aerodynamic loads on the drivetrain of a LHAWT.

In this instance some concluding remarks can be drawn. The angular speed of the HSS shows the same trend irrespective of the used law of brake releasing. The chosen law of brake releasing shows a considerable affect on the torsional angle of the HSS at the initial regime of the LHAWT start up. It has been observed that the transfer of transient fluctuations on the system behavior from the rotor to the drivetrain system is considerable but not in vice versa.

Even though the proposed methodology constitutes a good starting point to obtain a good understanding of the aeroelastic behavior of LHAWTs, in the future it will be necessary not only to expand the present ideas, but it will be necessary to add a model of the power generation dynamics and the interconnection dynamics to the electrical network or the dynamics associated to a system of hydrogen production based on wind energy. This study can be further extended to study the fatigue effects on the drivetrain components that are affected due to fluctuations of the aerodynamic loads.

7. REFERENCES

Baruh H. *Analytical dynamics*. McGraw Hill; 1999.

Burden R. L., Faires J. D. *Numerical analysis, eighth edition*. Thompson Brooks; 2005.

Carnahan B., Luther H. A., Wilkes J. O. *Applied numerical methods*. John Wiley & Sons; 1969.

Preidikman S., Gebhardt C. G., Brewer A. T., Roccia B. A. Aeroservoelastic analysis of large horizontal-axis wind turbines: a new methodology. *11th Pan-American Congress of Applied Mechanics, Foz do Iguaçu*; 2010.

Gebhardt C. G., Preidikman S., Massa J. C., Della Barca A. Interacciones aerodinámicas no-lineales e inestacionarias en turbinas eólicas de eje horizontal y de gran potencia. *Mecánica Computacional*; **28**: 1489-1505; 2009.

Gebhardt C. G., Preidikman S., Massa J. C. Numerical simulations of the aerodynamic behaviour of large horizontal-axis wind turbines. *International Journal of Hydrogen Energy* 2010; doi:10.1016/j.ijhydene.2009.12.089

Heat M. T. Scientific *computing an introduction survey, second edition*. McGraw Hill; 2002.

Kandil O. A, Mook D. T, Nayfeh A. H. Non–linear prediction of the aerodynamic loads on lifting surfaces. *Journal of Aircraft*; **13**, 22–28; 1976.

Katz J., Plotkin A. *Low–speed aerodynamics, second edition*. Cambridge University Press; 2001.

Konstandinopoulos P., Mook D. T., Nayfeh A. H. *A numerical method for general, unsteady aerodynamics*. AIAA–81–1877; 1981.

Lugt H. Vortex *flow in nature and technology*. John Wiley & Sons; 1983.

Preidikman S. *Numerical simulations of interactions among aerodynamics, structural dynamics, and control systems*. Ph.D. Thesis, Virginia Polytechnic Institute and State University; 1998.

Tenenbaum R. A. *Fundamentals of applied dynamics*. Springer-Verlag; 2004.